Available online at www.keaipublishing.com/en/journals/journal-of-magnesium-and-alloys/

ScienceDirect

Journal of Magnesium and Alloys 13 (2025) 3768–3783

www.elsevier.com/locate/jma

Full Length Article

Enhancing strength at elevated temperatures via dynamic high-density mobile dislocations in Mg alloys ☆

Mingyu Fan [a,b,c], Ye Cui [a,*], Xin Zhou [d,e], Junming Chen [a], Yang Zhang [a], Lixin Sun [a], Jamieson Brechtl [f], Daqing Fang [g], Qian Li [h,i], Qingqing Ding [j], Hongbin Bei [j], Peter K. Liaw [f], Yanzhuo Xue [k], Xun-Li Wang [b,c], Yang Lu [l,*], Zhongwu Zhang [a,*]

[a] *Key Laboratory of Superlight Materials and Surface Technology, Ministry of Education, College of Materials Science and Chemical Engineering, Harbin Engineering University, Harbin, 150001, China*

[b] *Department of Physics and Center for Neutron Scattering, City University of Hong Kong, Hong Kong, Kowloon, 999077, China*

[c] *Shenzhen Research Institute of City University of Hong Kong, Shenzhen Hi-Tech Industrial Park, Shenzhen, 518057, China*

[d] *Department of Mechanical Engineering, City University of Hong Kong, Kowloon, China*

[e] *Physikalisches Institut, Westfälische Wilhelms-Universität, Münster, 48149, Germany*

[f] *Department of Materials Science and Engineering, The University of Tennessee, Knoxville, TN 37996-2100, USA*

[g] *State Key Laboratory for Mechanical Behavior of Materials, School of Materials Science and Engineering, Xi'an Jiaotong University, Xi'an 710049, China*

[h] *National Engineering Research Center for Magnesium Alloy, Chongqing University, Chongqing 400044, China*

[i] *State Key Laboratory of Advanced Special Steels & Shanghai Key Laboratory of Advanced Ferrometallurgy & School of Materials Science and Engineering, Shanghai University, Shanghai 200444, China*

[j] *School of Materials Science and Engineering, Zhejiang University, Hangzhou 310027, China*

[k] *College of Shipbuilding Engineering, Harbin Engineering University, Harbin, 150001, China*

[l] *Department of Mechanical Engineering, The University of Hong Kong, Hong Kong 999077, China*

Received 11 November 2024; received in revised form 30 January 2025; accepted 10 March 2025

Available online 1 April 2025

Abstract

Dislocation strengthening, as one of the methods to simultaneously enhance the room temperature strength and ductility of alloys, does not achieve the desired strengthening and plasticity effect during elevated-temperature deformation. Here, we report a novel strategy to boost the dislocation multiplication and accumulation during deformation at elevated temperatures through dynamic strain aging (DSA). With the introduction of the rare-earth element Ho in Mg-Y-Zn alloy, Ho atoms diffuse toward dislocations during deformation at elevated temperatures, provoking the DSA effect, which increases the dislocation density significantly via the interactions of mobile dislocations and Ho atoms. The resulting alloy achieves a great enhancement of dislocation hardening and obtains the dual benefits of high strength and good ductility simultaneously at high homologous temperatures. The present work provides an effective strategy to enhancing the strength and ductility for elevated-temperature materials.

Keywords: Mg-Y-Zn alloy; Ho addition; High-density mobile dislocations; Dynamic strain aging (DSA); Elevated-temperature strength.

1. Introduction

Improving both strength and ductility is a key issue in structural materials, specifically at elevated temperatures [1–3]. In general, the improvement in strength is usually accompanied by the loss of ductility, which is the so-called strength-ductility trade-off dilemma [4]. To solve

☆ Peer review under the responsibility of Chongqing University.

* Corresponding authors. Key Laboratory of Superlight Materials and Surface Technology, Ministry of Education, College of Materials Science and Chemical Engineering, Harbin Engineering University, Harbin, 150001, China.

E-mail addresses: cuiye@hrbeu.edu.cn (Y. Cui), ylu1@hku.hk (Y. Lu), zwzhang@hrbeu.edu.cn (Z. Zhang).

https://doi.org/10.1016/j.jma.2025.03.004

this problem, numerous strategies have been developed, such as grain-boundaries strengthening [5,6], coherent twin-boundaries strengthening [7], dislocation hardening [2], and nanoprecipitation strengthening [8,9]. Amongst them, He et al. [2] reported that high-density dislocations in martensite contribute to room-temperature strength, while mobile dislocations in martensite promote high ductility. Based upon the Taylor hardening law, once dislocation hardening is activated, the strength of materials monotonically increases with the increase of the dislocation density [10].

In the past decades, a variety of unique dislocation structures were introduced, achieving an excellent combination of strength and ductility [2,8,11,12], e.g., the novel gradient nano-scaled dislocation-cell structures [13], the complex dislocation network with formed Lomer locks [14], and high-density dislocations originated from severe plastic deformation or phase transformation [2,15]. However, it is believed that the dislocation hardening is not suitable for elevated-temperature materials due to the decrease in the dislocation density, which is caused by recovery and recrystallization at elevated temperatures [16–18]. Metallic materials inevitably exhibit reduced strength at elevated temperatures. Although precipitation strengthening and solid solution strengthening can enhance the elevated-temperature mechanical properties of alloys by unique alloy composition designs to achieve high thermal stability of precipitates and high solute atom concentrations, traditional alloy designs are often not aimed at controlling the high thermal stability of precipitates and high solute atom concentrations, leading to undesirable elevated-temperature mechanical properties. Therefore, improving both strength and ductility prosperities of the traditional metallic structural materials during the elevated-temperature process is highly desirable, while remaining a great challenge.

It is reported that dynamic strain aging (DSA) effect can promote mobile dislocation multiplication [19,20]. The nature of DSA is the interaction between the diffusional solute atoms and dislocations through repeated pinning and unpinning, generating high-density dislocations [20–29]. The DSA is commonly found in various alloys, such as steels [19], aluminum alloys [22], magnesium alloys [24], and nickel-based superalloys [25]. The rare-earth (RE) elements (Y, Gd, and Nd) are beneficial to the activation of DSA effects in magnesium (Mg) alloys [30–32], in this type of Mg alloys, although it provides large elevated-temperature ductility, the strength improvement is weak. The RE element of Ho possesses similar physical properties to Y, Gd, and Nd. However, the solid solubility of Ho in the Mg matrix (5.44 at.%, atomic percent) is far higher than that of Y (3.75 at.%). Thus, Ho is a promising candidate to promote the DSA effect, activating a remarkable dislocation multiplication and promoting strain hardening. Additionally, Ho has the ability to reduce stacking fault energy, activate $\langle c + a \rangle$ dislocations, and help alleviate the localized strain variation issues caused by traditional DSA [33].

Inspired by the above-mentioned merits, a strategy was developed to achieve the high-density dislocations during elevated-temperature deformation through the mobile dislocation multiplication by DSA. In this strategy, Ho is introduced in Mg-Y-Zn-based alloys containing the long-period stacking-ordered (LPSO) phase. The DSA effect induced by Ho brings about high-density dislocation multiplication in the sample during tension at elevated temperatures. Large amount of dislocation accumulation and their interactions with the LPSO phase predominantly contribute excellent strain hardening, resulting in the enhanced elevated temperature strength and ductility. The unique features enable the increases of both strength-ductility of Mg alloys at elevated temperatures, and are also applicable to other alloy systems.

2. Material and methods

2.1. Sample preparation

The Mg-Y-Zn and Mg-Y-Zn-Ho as-cast ingots were prepared by pure Mg (99.99 wt percent, wt.%), pure Zn (99.9 wt.%), Mg-Ho (20 wt.%) master alloy, and Mg-Y (20 wt.%) master alloy. The master alloys, pure Mg, and pure Zn were melted in a mild steel crucible at 750 °C under the inert atmosphere of Ar. The resulting melt was transferred into the cooling crystallizer at 710 °C. The semi-continuous casting process was conducted at a speed of circa (ca.) 100 mm/min. Three samples with chemical compositions (at.%) of $Mg_{96}Y_1Zn_1Ho_2$, $Mg_{97}Y_1Zn_1Ho_1$, and $Mg_{98}Y_1Zn_1$ were produced.

2.2. Material characterization

The structures of the alloys were characterized by scanning electron microscopy (SEM, Thermo scientific Apreo S LoVac) and transmission electron microscopy (TEM, FEI, Talos F200X G2), as well as high-angle annular dark-field scanning transmission electron microscopy (The atomic resolution HAADF-STEM) mode (JEOL-ARM200F with spherical aberration correctors). The surfaces of the SEM samples were mechanically polished and etched in a 4-volume percent (vol.%) nital solution. The TEM samples were prepared by mechanical grinding, followed by low-angle (3°–9°) ion milling, using the Gatan 691 precision argon ion-polishing system. Based electron back scatter dffraction (EBSD) data [34], The AZtec software was used to quantify the orientation differences between two points near the LPSO phase to characterize dislocation accumulation. Phase identification and dislocation densities were performed by X-ray diffraction (XRD) on an X'Pert Pro X diffractometer employing Cu K_a ($\lambda = 0.15406$ nm). The diffraction lines were recorded at 40 kV and 150 mA from 30 to 80° with a step of 0.0065° (2θ). The quantitative analyses of dislocation densities were performed, based on the XRD data of the tested tensile samples, using the variance method [35]. The diffraction lines were recorded from 30 to 80° with a step of 0.0065°(2θ). For this method, the following mathematical relation is used to relate the kth-order restricted moment and dislocation den-

sity (ρ), and is given by:

$$M_2(q) = \frac{1}{\pi^2 \varepsilon_F} q - \frac{L}{4\pi^2 K^2 \varepsilon_F^2} + \frac{\chi \rho}{2\pi^2} \ln(q/q_0) \quad (1)$$

$q = 2/\lambda[Sin\theta_1\text{-}Sin\theta_0]$, θ_1 is the diffraction angle, and θ_0 is the Bragg angle. ε_F is the average coherent domain size. $\chi = (\pi/2) b^2 g^2 C$, C is 0.2075 for Mg alloy. Regression analysis of the plot for $M_2(q)$ vs. $\ln(q/q_0)$ gives the values of ρ from the slope. The kth-order restricted moment, is calculated through the following equation [36]:

$$M_k(q) = \frac{\int_{-q}^{q} q^k I(q) dq}{\int_{-\infty}^{\infty} I(q) dq} \quad (2)$$

g represents the magnitude of the diffraction vector for the X-ray reflection, and C is average contrast factor [37]), and b is the magnitude of the Burger's vector (considered as 0.32 nm for magnesium alloys [38]). To reduce dislocation calculation errors, the reference sample was prepared through recrystallizing the $Mg_{97}Y_1Zn_1Ho_1$ and $Mg_{96}Y_1Zn_1Ho_2$ alloys at 350 °C for 10 h.

To elucidate the interaction between Cottrell atmosphere of Ho atoms and dislocation phases, the molecular dynamics (MD) simulations were conducted to analyze the deformation mechanisms of $Mg_{96}Y_1Zn_1Ho_2$ alloys under a strain rate of 10^9 s^{-1} at 200 °C. It has been reported that a strain rate of 10^9 s^{-1} can be considered a quasi-static loading rate. The strain rates used in this work (5×10^{-4} s^{-1} to 5×10^{-3} s^{-1}) fall within the quasi-static stretching rate range. Therefore, a strain rate of 10^9 s^{-1} was selected for the molecular dynamics simulations [39]. These MD simulations were conducted with the assistance of open-source codes OVITO and the parallel molecular dynamics code LAMMPS [40]. The atomic potential chosen is the modified embedded atom method (MEAM) interatomic potential for Mg-Y [41].

Tensile tests were conducted on an Instron 5869 tester at room temperature (RT) and various elevated temperatures (100–300 °C). Samples, with a gauge size of 20 mm × 4 mm × 1 mm, were cut by an electro-discharging machine, followed by mechanical polishing with a surface roughness of 6.5 μm. For the elevated-temperature testing, the samples were placed in an elevated-temperature furnace that has been heated to the target temperatures (100–300 °C) and held for 5 min before testing. The nominal strain rates were selected in the range of 5×10^{-4} s^{-1} - 5×10^{-3} s^{-1}. Hardness measurements of matrix were conducted on an HXS-1000Z tester under an applied load of 10 g and dwell time of 15 s. Each data point reported represents an average of at least 10 measurements. The hardness of the LPSO phase was measured via nano-indentation (Agilent G200) at room temperature using a Berkovich diamond indenter of a maximum depth of 500 nm. The strain mapping of each sample was analyzed through Digital Image Correlation (DIC) during in-situ loading.

3. Results

3.1. Mechanical properties

The engineering tensile stress-strain curves of the as-cast Mg-Y-Zn and Mg-Y-Zn-Ho alloys obtained at room temperature (RT) and 200 °C are shown in Fig. 1a. At RT, the tensile strength was enhanced slightly along with a reduction in the elongation with the addition of Ho. When the temperature increased to 200 °C, the strength of the Mg-Y-Zn alloy decreased along with the increase of elongation compared with those at RT, agree with the usual trend of elevated temperature deformation. Surprisingly, both the strength and elongation of the Ho-containing Mg alloys increased significantly at 200 °C when compared with their counterparts at RT, differing from the pristine Mg alloy. The tensile strength and elongation of the as-cast $Mg_{96}Y_1Zn_1Ho_2$ (at.%) alloy at 200 °C are 230 MPa and 21%, respectively, both of which are much higher than those at RT (179 MPa and 9%, respectively). It is found that with the increase in experimental temperature, the strength of the Mg-Y-Zn alloy decreases while its ductility improves, whereas both the strength and ductility of the Mg-Y-Zn-Ho alloy increase simultaneously. These results indicate that the addition of Ho can enhance both strength and elongation simultaneously at elevated temperatures. Moreover, the tensile curves of Ho-containing Mg alloys, especially the $Mg_{96}Y_1Zn_1Ho_2$ alloy showing serration phenomena during elevated-temperature deformation, while Mg alloys without Ho show a smooth tensile curve in the whole range of strain. The serration induced by the addition of Ho atoms in Mg-Y-Zn alloys may be the key to the improvement of mechanical properties at elevated temperatures. The serration phenomena may be mainly related to the pinning and unpinning processes of Ho atoms and dislocations during the deformation of the alloy, i.e., DSA.

To verify the DSA effect of the Ho addition in the Mg-Y-Zn-based alloys at elevated temperatures, the tensile stress-strain curves of the $Mg_{96}Y_1Zn_1Ho_2$ alloy were obtained at various strain rates at 200 °C and various temperatures at rate of 1×10^{-3} s^{-1}, as exhibited in Fig. 1c-f. For various given strain rates, observable serrations appear after critical strains, as indicated by stars in Fig. 1d. The critical strain increases with the increase of the strain rate. At various elevated temperatures, both the tensile strength and elongation increase significantly, as compared to that at RT. The flow curve is smooth when tested below 100 °C. However, serration behavior occurs beyond a critical strain, ε_c, when experimented at elevated temperatures above 150 °C. The critical strain, ε_c, decreases with the increase in the test temperatures, as shown in Fig. 1(f). During the occurrence of DSA, the critical strain is negatively correlated with temperature, as the critical strain decreases with increasing temperature. This process is mainly related to the interaction between solid solution atoms and dislocations [21]. With the increase in temperature, the diffusion rate of Ho atoms increases, causing the Ho atoms to pin dislocations in advance, thereby leading to a decrease in critical strain. These results confirm that the addition of Ho

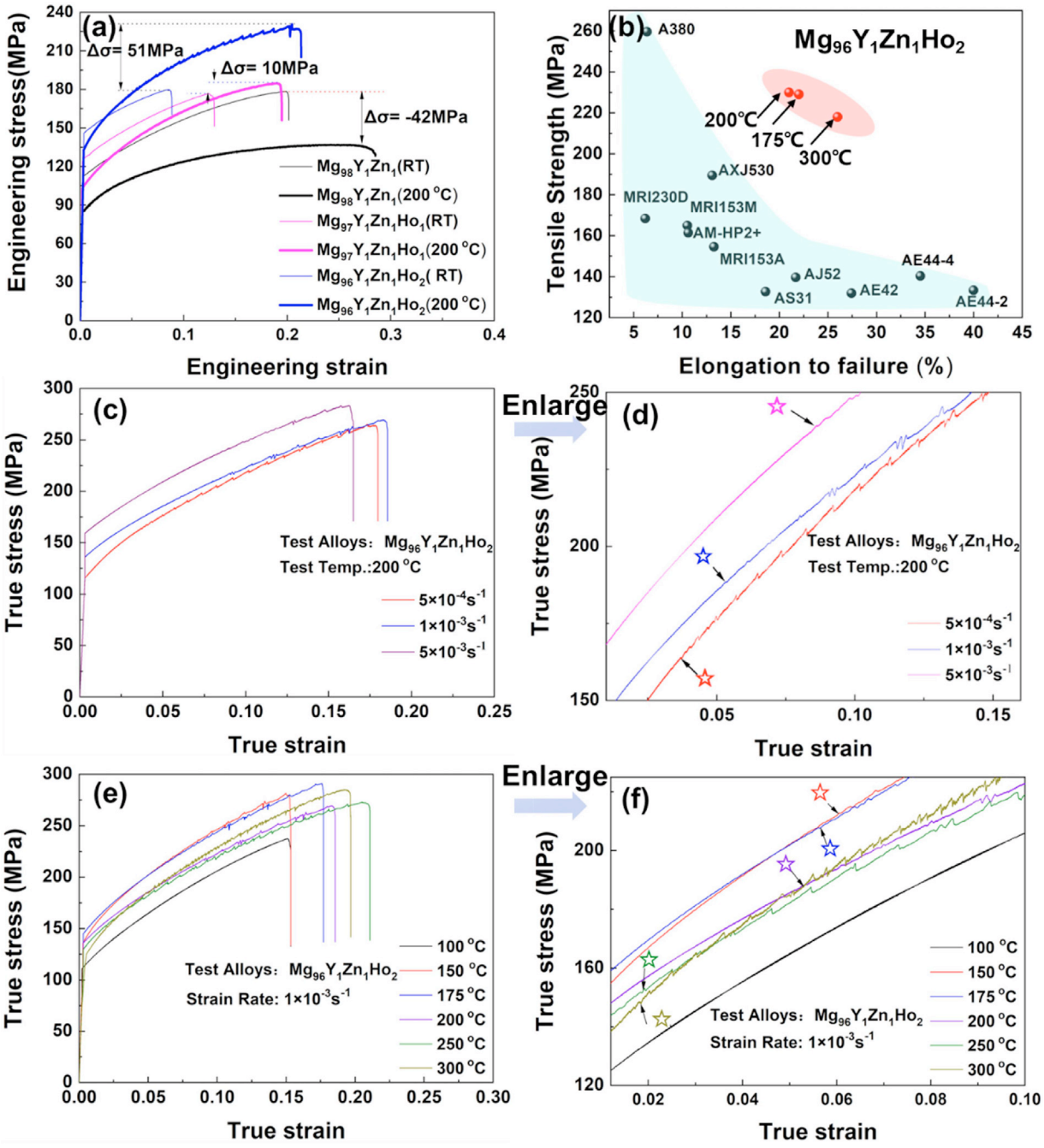

Fig. 1. Mechanical properties of the as-cast Mg-Y-Zn and Mg-Y-Zn-Ho alloys. (a) Engineering tensile stress-strain curves of the Mg-Y-Zn and Mg-Y-Zn-Ho alloys at RT and 200 °C; (b) Some other as-cast Mg alloys [40] (at 175 °C), (c) Tensile stress-stain curves of $Mg_{96}Y_1Zn_1Ho_2$ tested at 200 °C with various strain rates; (d) Critical strains for the occurrence of the DSA effect in (c); (e) Tensile stress-stain curves of $Mg_{96}Y_1Zn_1Ho_2$ experimented at various temperatures with a strain rate of 1×10^{-3} s^{-1}; (f) Critical strains for the occurrence of the DSA effect in (e). The critical strains are indicated by star marks.

activates the DSA effect at elevated temperatures. Decreasing strain rate or elevating deformation temperature promotes the diffusion of Ho atoms to dislocations, leading to a decrease of the critical strain for activating the DSA effect. Based on our tensile tests at various temperatures, we summarized the mechanical properties of the $Mg_{96}Y_1Zn_1Ho_2$ tested at 175 °C, 200 °C and 300 °C along with some other as-cast Mg alloys in literature [42] tested at 175 °C are summarized in Fig. 1b. One can see the as-cast Ho-containing Mg-Y-Zn alloys exhibit excellent mechanical properties with activation of the DSA effect, even as the environmental temperature rise to 300 °C (as high as ~$0.62T_m$).

3.2. Microstructural characteristics before and after tension

In general, primary phases, dynamic precipitation, and grain size may affect the mechanical properties of the alloy. The SEM micrographs of the Mg-Y-Zn and Mg-Y-Zn-Ho

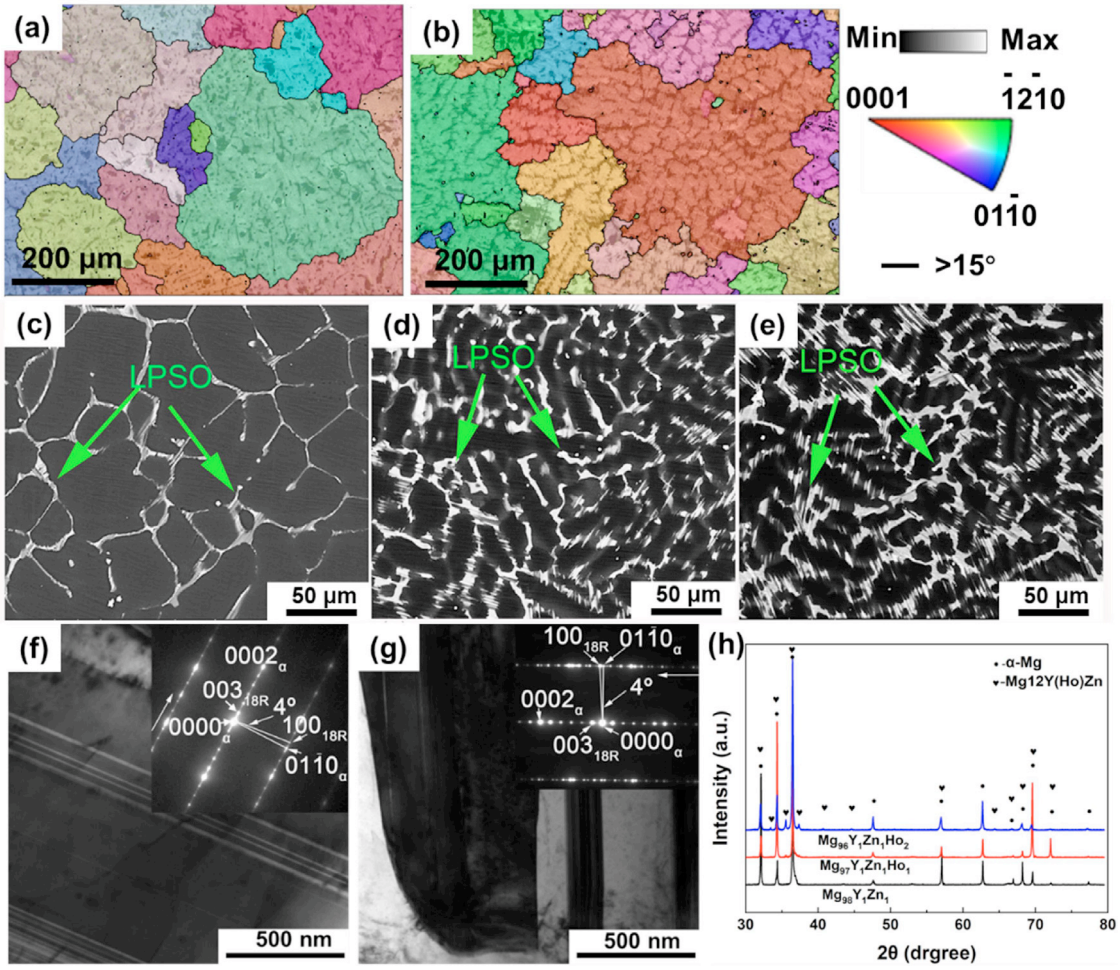

Fig. 2. Microstructures of the as-cast Mg-Y-Zn and Mg-Y-Zn-Ho alloys. (a) EBSD map of Mg-Y-Zn, (b) EBSD map of $Mg_{96}Y_1Zn_1Ho_2$, (c) SEM microstructure images of Mg-Y-Zn, (d) SEM microstructure images of $Mg_{97}Y_1Zn_1Ho_1$, and (e) SEM microstructure images of $Mg_{96}Y_1Zn_1Ho_2$ and bright-field TEM images of as-cast (f) $Mg_{97}Y_1Zn_1$ and (g) $Mg_{96}Y_1Zn_1Ho_2$ alloys, (h) XRD patterns of the as-cast Mg-Y-Zn and Mg-Y-Zn-Ho alloys.

alloys are presented in Fig.2c and d. Both Mg-Y-Zn and Mg-Y-Zn-Ho alloys are composed of the black Mg matrix and the second phase in grey. The XRD patterns are displayed in Fig. 2f. The Second phase in both alloys with and without Ho is the LPSO phase (peaks at 35.4° and 37.3°), which match the peak positions of the LPSO phase reported in the literature [12]. The XRD patterns of the as-cast $Mg_{96}Y_1Zn_1Ho_2$ alloys before and after deformation are shown in Fig. 3. No new phases are formed during elevated-temperature deformation.

The EBSD map of the $Mg_{98}Y_1Zn_1$ and $Mg_{96}Y_1Zn_1Ho_2$ alloys are presented in Fig.2a and b. It is found that both cast alloys ($Mg_{98}Y_1Zn_1$ and $Mg_{96}Y_1Zn_1Ho_2$ alloys) have large grains, which are mainly composed of many fine effective grains with a similar crystal orientation. The fine effective grains in one large grain are separated by the second phases in a net-like structure. The statistical analysis shows that fine effective grains size of the $Mg_{98}Y_1Zn_1$, $Mg_{97}Y_1Zn_1Ho_1$ and $Mg_{96}Y_1Zn_1Ho_2$ alloys are 50 μm, 30 μm, and 27 μm, respectively. For the $Mg_{97}Y_1Zn_1Ho_1$ and $Mg_{96}Y_1Zn_1Ho_2$ alloys, the grain size is close to each other, but elevated-temperatures mechanical properties are significantly different, which means that the abnormally enhanced elevated temperature mechanical properties of Ho-containing alloys do not come from the effect of grain size.

To further verify whether twinning contributes additional work hardening, EBSD was used to analyze the microstructure of $Mg_{98}Y_1Zn_1$ and $Mg_{96}Y_1Zn_1Ho_2$ alloys after 8% deformation, as shown in Fig. 4. Since The $\{10\bar{1}2\}$ extension twin and $\{10\bar{1}1\}$ contraction twin are common twinning modes [45], these two modes of twinning were analyzed. It is evident that the boundary with a misorientation of $<1\bar{2}10>$ 86.3° is associated with $\{10\bar{1}2\}$ extension twin, whereas the boundary with a misorientation of $<1\bar{2}10>$ 56° is linked to $\{10\bar{1}1\}$ contraction twin. It was found that both $Mg_{98}Y_1Zn_1$ and $Mg_{96}Y_1Zn_1Ho_2$ alloys exhibit tensile twin, with the volume fraction of twins being similar (16% and 18%, respectively). Therefore, the EBSD analysis indicates that twinning is not the main reason for the additional work hardening.

The hardness of the Mg matrix and the LPSO phase in Mg-Y-Zn and Mg-Y-Zn-Ho alloys is presented in Fig. 5. The hardness of the Mg matrix increases with the addition of Ho, indicating that the addition of Ho can strengthen the

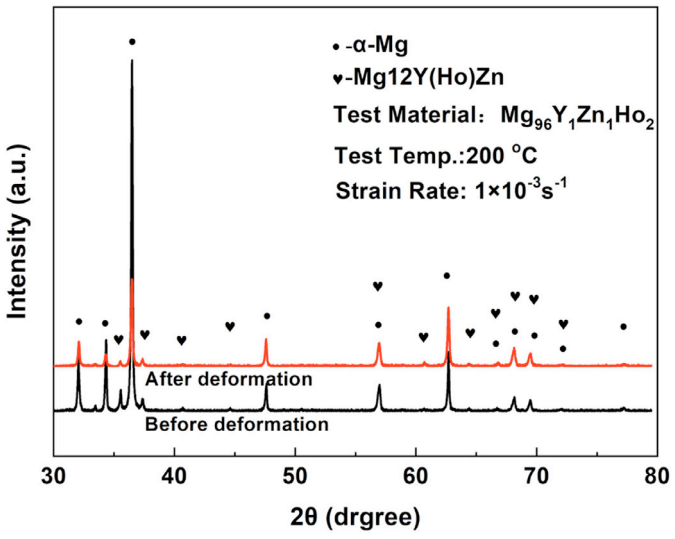

Fig. 3. XRD patterns before and after deformation in the as-cast $Mg_{96}Y_1Zn_1Ho_2$ alloys.

alloy through solid-solution strengthening. Compared with the Mg-Y-Zn alloy, the addition of Ho also can strengthen the alloy through solid solutions, and the increase of the RT strength of $Mg_{97}Y_1Zn_1Ho_1$ and $Mg_{96}Y_1Zn_1Ho_2$ alloys is due to Ho-atoms solid-solution strengthening, However, the increase of the RT strength [4 MPa from Fig. 1a] of the two alloys is much lower than the increase of the elevated-temperature strength [44 MPa from Fig. 1a]. Therefore, Ho-atoms-solution strengthening is not the main reason for the elevated-temperature strength.

The measured volume fractions of the LPSO phase in Mg-Y-Zn, $Mg_{97}Y_1Zn_1Ho_1$, and $Mg_{96}Y_1Zn_1Ho_2$ alloys are ~ 11%, ~ 29%, and ~ 29%, respectively, indicating that the addition of Ho increased the LPSO content significantly. But the distribution of the LPSO phase in $Mg_{97}Y_1Zn_1Ho_1$ and $Mg_{96}Y_1Zn_1Ho_2$ alloys is similar. On the other hand, the change of hardness of the LPSO phase can be negligible with the addition of Ho (Fig. 5b). The transmission electron microscopy bright-field (TEM-BF) images of $Mg_{97}Y_1Zn_1$ and $Mg_{96}Y_1Zn_1Ho_2$ alloys are displayed in Fig. 2f and g, respectively. The corresponding selected area electron diffraction (SAED) patterns of the LPSO phases are presented as insets. Five extra diffraction spots are appearing at positions, n/6, of the diffraction pattern in Mg-Y-Zn and Mg-Y-Zn-Ho alloys, confirming that the LPSO phase in both Mg-Y-Zn and Mg-Y-Zn-Ho alloys is a 18R LPSO phase [43,44]. To investigate the effect of the LPSO phase on elevated-temperature strength, a comparison was made between the LPSO phase volume fraction and the hardness of $Mg_{97}Y_1Zn_1Ho_1$ and $Mg_{96}Y_1Zn_1Ho_2$ alloys. It was found that the volume fraction (29% and 29%, respectively), hardness (1.36±0.29 GPa and 1.38±0,20 GPa, respectively), and composition (Table 1) of the LPSO phase are identical in both alloys. However, the elevated-temperature strength of $Mg_{96}Y_1Zn_1Ho_2$ alloy is significantly higher than that of $Mg_{97}Y_1Zn_1Ho_1$ alloy. These results indicate that the addition of Ho does not affect the structure and hardness of the LPSO phase, which implicates LPSO is not the direct reason for the abnormally enhanced elevated-temperature mechanical properties of Ho-containing alloys.

The distribution of elements in $Mg_{97}Y_1Zn_1Ho_1$ and $Mg_{96}Y_1Zn_1Ho_2$ alloys are determined by the TEM/EDS, as presented in Fig. 6. The contents of Ho, Y, and Zn in LPSO are much higher than that in the Mg matrix. The Ho contents of LPSO in $Mg_{97}Y_1Zn_1Ho_1$ and $Mg_{96}Y_1Zn_1Ho_2$ are 2.5 at.%, and 4.5 at.%, respectively. At the same time, the (Ho,Y)/Zn atomic ratio in the $Mg_{98}Y_1Zn_1$, $Mg_{97}Y_1Zn1Ho_1$, and $Mg_{96}Y_1Zn_1Ho_2$ alloys is close to 1:1, corresponding to the chemical composition of the LPSO phase. The content of Ho in the $Mg_{96}Y_1Zn_1Ho_2$ matrix (1.4 at.%) is ca. 3 times in $Mg_{97}Y_1Zn_1Ho_1$ (0.5 at.%). The detailed elemental contents are exhibited in Table 1. This result is consistent with the

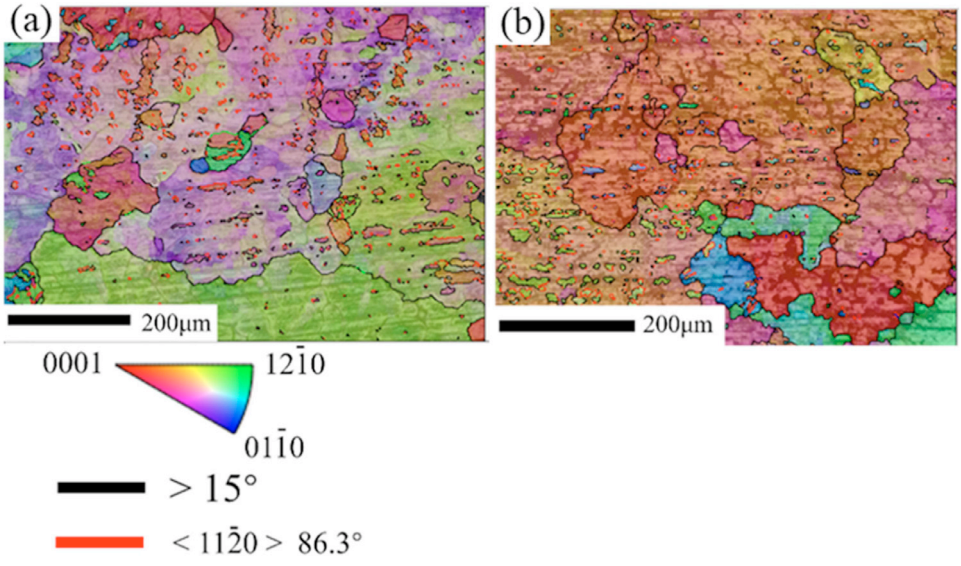

Fig. 4. The EBSD analysis of (a) 8%-strained $Mg_{98}Y_1Zn_1$ alloy and (b) 8%-strained $Mg_{96}Y_1Zn_1Ho_2$ alloy at 200 °C.

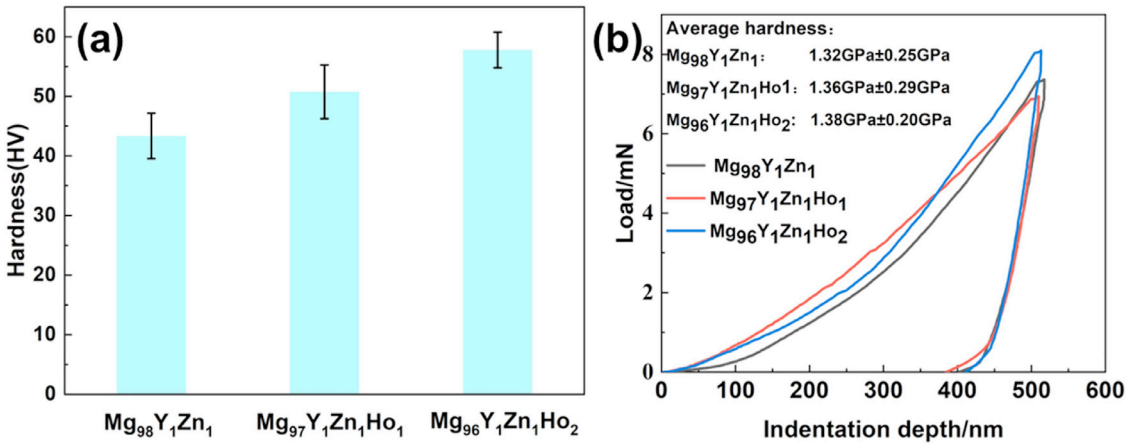

Fig. 5. The hardness of the (a) matrix and (b) LPSO phase in the as-cast Mg-Y-Zn and Mg-Y-Zn-Ho alloys.

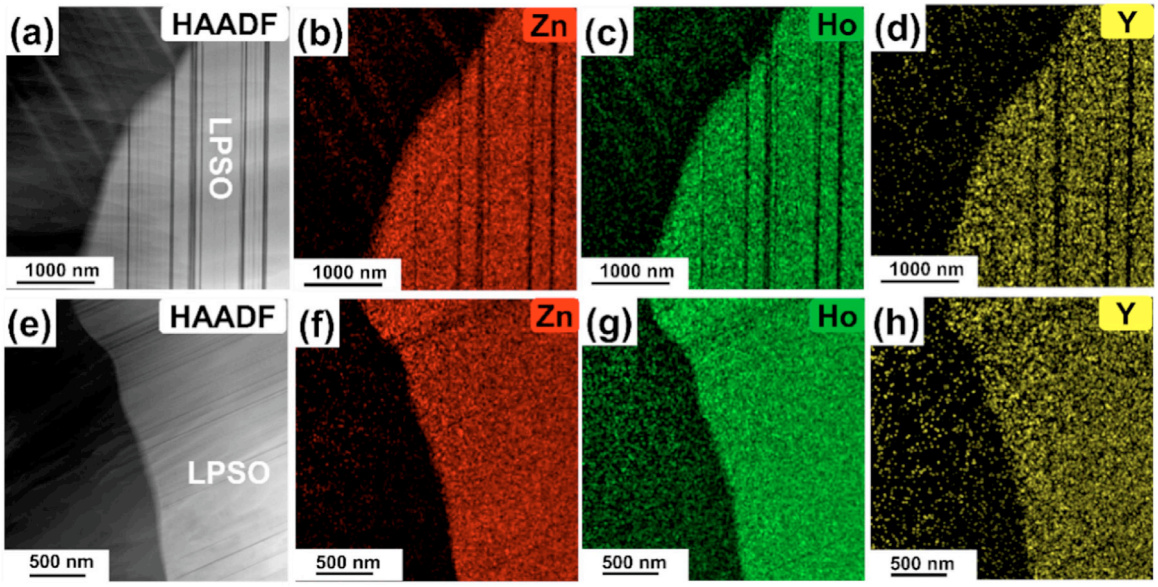

Fig. 6. HAADF-TEM/EDS images and the distribution of elements of (a)–(d) the as-cast $Mg_{97}Y_1Zn_1Ho_1$ and (e)–(h) $Mg_{96}Y_1Zn_1Ho_2$.

Table 1
Chemical compositions of the primary phases in $Mg_{97}Y_1Zn_1Ho_1$ and $Mg_{96}Y_1Zn_1Ho_2$ alloys.

Element		at.%				wt.%			
		Mg	Y	Zn	Ho	Mg	Y	Zn	Ho
$Mg_{98}Y_1Zn_1$	LPSO	88.3	5.5	6.2	-	70.6	16.1	13.3	-
$Mg_{97}Y_1Zn_1Ho_1$	Mg matrix	98.6	0.4	0.5	0.5	94.7	1.3	1.3	2.7
	LPSO	88.7	2.7	6.1	2.5	68.7	7.1	12.2	12.0
$Mg_{96}Y_1Zn_1Ho_2$	Mg matrix	97.6	0.7	0.3	1.4	89.1	2.0	0.7	8.2
	LPSO	87.0	2.6	5.9	4.5	62.5	6.4	10.9	20.2

hardness data, i.e., the solution of Ho in the Mg matrix enhances the hardness, as shown in Fig. 5a.

The TEM bright-field images of the as-cast $Mg_{98}Y_1Zn_1$ and $Mg_{96}Y_1Zn_1Ho_2$ after tensile-deforming with a strain of 8% at RT and 200 °C are shown in Fig. 7. Many dislocation tangles exist whether the deformation of $Mg_{96}Y_1Zn_1Ho_2$ is 8% at RT or the deformation of $Mg_{98}Y_1Zn_1$ is 8% at 200 °C, while a large amount of uniform mobile dislocations of $Mg_{96}Y_1Zn_1Ho_2$ form at 200 °C, as indicated by the white arrows in Fig. 7a, b and c, respectively. During the occurrence of DSA, when mobile dislocations are pinned by solute atoms, these dislocations become temporarily locked. As subsequent dislocations continue to move, the repulsive force between the dislocations increases, which in turn acts on the pinned dislocations, causing them to break free from the solute atoms' pinning. This results in the formation of mo-

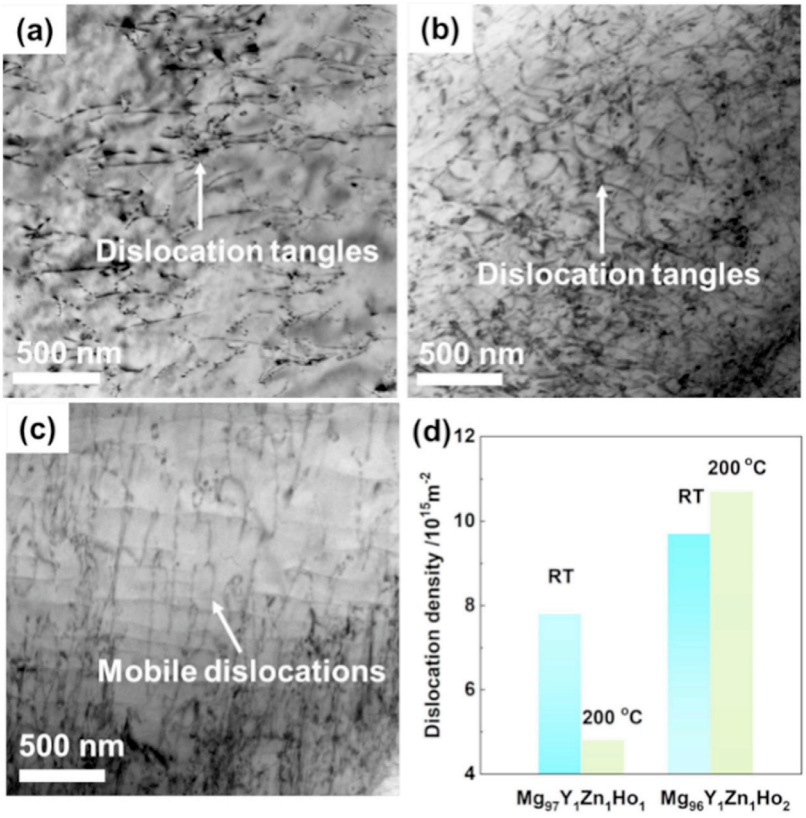

Fig. 7. TEM bright-field image of dislocation configuration in the as-cast alloys for a tensile strain of 8%: (a) $Mg_{98}Y_1Zn_1$ at 200 °C, (b) $Mg_{96}Y_1Zn_1Ho_2$ at RT, and (c) $Mg_{96}Y_1Zn_1Ho_2$ at 200 °C. The beam direction in (a), (b), and (c) is $[2\bar{1}\bar{1}0]$. (d) The dislocation densities of the 8%-strained Mg-Y-Zn-Ho alloys, calculated from the full width at half maxima (FWHM) of {102} and {103} X-ray diffraction peaks.

bile dislocations at the microstructural level. When DSA has not occurred, mobile dislocations are pinned by immobile dislocations. Unlike solute atoms, immobile dislocations cannot be easily detached from the pinned dislocations. Therefore, when subsequent dislocations continue to move, the pinned dislocations remain locked, resulting in the formation of a dislocation entanglements structure. In order to further analyze the dislocation types, two-beam bright conditions for TEM were used for dislocation observation. Based on the invisibility criterion of $g \cdot b = 0$ [45], where g and b represent the reflection and Burgers vector, respectively. When a particular reflection vector is set as $g = 0002$, $\langle c \rangle$ dislocations and $\langle c + a \rangle$ dislocations are visible, while $\langle a \rangle$ dislocations are invisible. In contrast, when the reflection vector is set as $g = 01\bar{1}0$, the $\langle a \rangle$ and $<c + a>$dislocations become visible, while $\langle c \rangle$ dislocations are invisible. The dislocation configuration of the cast $Mg_{96}Y_1Zn_1Ho_2$ alloy deformed by 8% at 200 °C is shown in Fig. 8. The bright field images with zone axis of $[2\bar{1}\bar{1}0]$ is shown in Fig. 8a and b, it is found that there are some dislocations. However, dislocations are visible with the reflection vector of $g = 0002$, as shown in Fig. 8c and d, indicating that there are $\langle c + a \rangle$ dislocations. Dislocations are visible with the reflection vector of $g = 01\bar{1}0$, as shown in Fig. 8e and Fig. 8f, indicating that basal $\langle a \rangle$ dislocations, marked by the white arrows. The Burgers vector of the basal $\langle a \rangle$ dislocations in Mg alloy is $1/2 < 2\bar{1}\bar{1}0>$. Moreover, the basal $<a>$dislocations direction are parallel to the $<01\bar{1}0>$ direction and are mixed dislocations, which has been reported in the literature to interact with solute atoms and promote DSA [24]. The dislocation densities in $Mg_{97}Y_1Zn_1Ho_1$ and $Mg_{96}Y_1Zn_1Ho_2$ after an 8% strain at RT and 200 °C are shown in Fig. 7d, which are calculated based on XRD patterns shown in Fig. 9. $Mg_{97}Y_1Zn_1Ho_1$ possesses a dislocation density of 5.1×10^{15} m^{-2} and 1.8×10^{15} m^{-2} after tensile straining at RT and 200 °C, respectively. While for the $Mg_{97}Y_1Zn_1Ho_2$ alloy, the dislocation densities are 7.2×10^{15} m^{-2} and 1.4×10^{16} m^{-2}, respectively. As observed in the tensile curves, $Mg_{97}Y_1Zn_1Ho_1$ and $Mg_{96}Y_1Zn_1Ho_2$ alloys have no DSA effect at RT. At 200 °C, $Mg_{97}Y_1Zn_1Ho_1$ does not exhibit a DSA effect when deformed at a plastic strain of 8%. While the $Mg_{96}Y_1Zn_1Ho_2$ alloy exhibits an obvious DSA effect when deformed at the plastic strain of 8%. It is obvious that the $Mg_{96}Y_1Zn_1Ho_2$ alloy significantly increases the dislocation density by the DSA.

In $Mg_{97}Y_1Zn_1Ho_1$ alloy during elevated-temperature deformation, the DSA effect also occurs, but the content of Ho atoms in the matrix is low, leading to fewer Ho atoms diffusing to the vicinity of dislocations for pinning and unpinning, fewer dislocation multiplication, and a dislocation density lower than that at elevated temperatures, compared to room temperature. In $Mg_{96}Y_1Zn_1Ho_2$ alloy, the matrix contains a sufficient amount of Ho atoms, greatly activating DSA, pro-

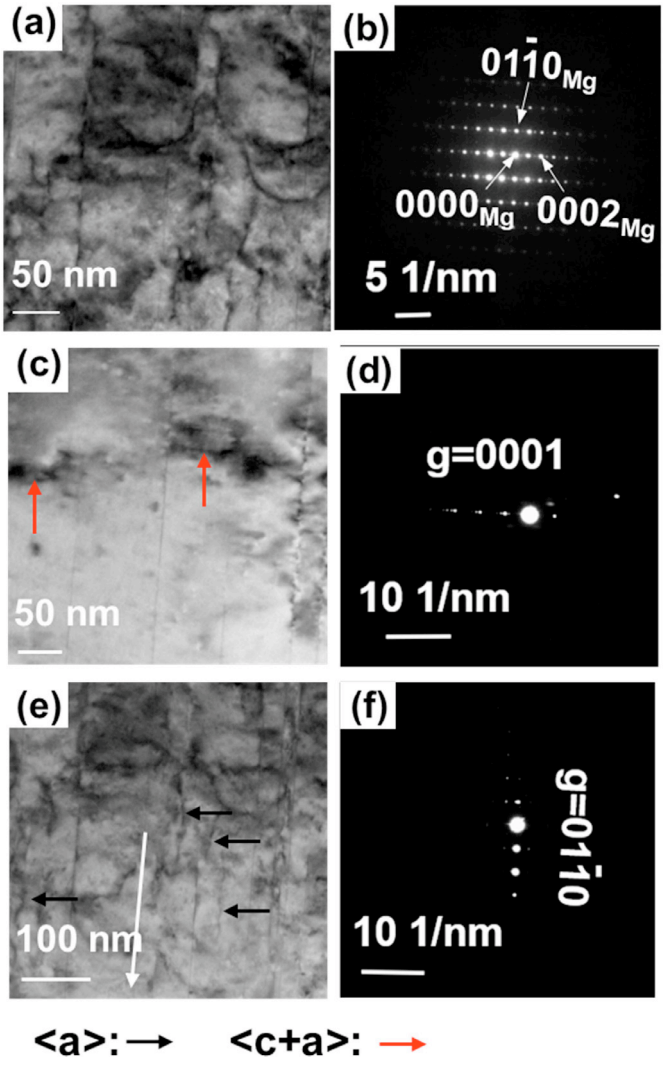

Fig. 8. Dislocation configurations in the tensile-deformed-8% $Mg_{96}Y_1Zn_1Ho_2$ alloy at 200 °C. (a) TEM bright-field images with zone axis of $[2\bar{1}\bar{1}0]$ and corresponding to electron diffraction pattern (b); (c) and (d) TEM bright-field images viewed with $g = 0002$; (e) and (f) TEM dark-field images viewed with $g = 01\bar{1}0$.

moting significant dislocation multiplication, with the quantity of dislocation multiplication exceeding that of dislocation recovery. As a result, the elevated-temperature dislocation density is higher than the room temperature dislocation density.

Based on above observations, the abnormally enhanced elevated-temperature mechanical properties of the Ho-containing Mg-Y-Zn based alloys compared to their counterparts at RT are hardly attributed to the solute solution effect, LPSO phase, dynamic precipitation and grain size, but DSA induced by Ho at elevated temperatures, which promotes dislocation multiplication and indirectly strengthens the interactions of dislocations and LPSO phases/grain boundaries/solutes.

4. Discussions

4.1. Ho promotes DSA effect

To gain insight into the effect of Ho on the DSA mechanisms, the activation energy for the serrated flow of $Mg_{96}Y_1Zn_1Ho_2$ is evaluated based on the measured critical strain values in Fig. 1c-f. The critical strain is a remarkable feature of the serrated flow, strongly depending on the strain rate and testing temperature. The critical strain for DSA effect, ε_c, is generally expressed as Eq. (3) [46]:

$$\varepsilon_c^{m+\beta} = KT\,\dot{\varepsilon}\exp\left(\frac{Q}{RT}\right) \tag{3}$$

where Q is the activation energy at the onset of serrations, which is mainly related to the diffusion of a pinning atom, $\dot{\varepsilon}$ is the strain rate, R is the universal gas constant (8.3144 J/mol), T is the absolute temperature, m and β are exponents related to the vacancy concentration and mobile dislocation density, respectively, and K is a constant. The results of the correlation analysis for the critical strain and the strain rate of the $Mg_{96}Y_1Zn_1Ho_2$ alloy are presented in Fig. 10a and b, from which $(m+\beta)$ can be determined as 3.2. The apparent activation energy for the serrated flow is determined to be 64 kJ/mol, which is lower than that of the WE54 alloy (75 kJ/mol) [47]. The apparent activation energy

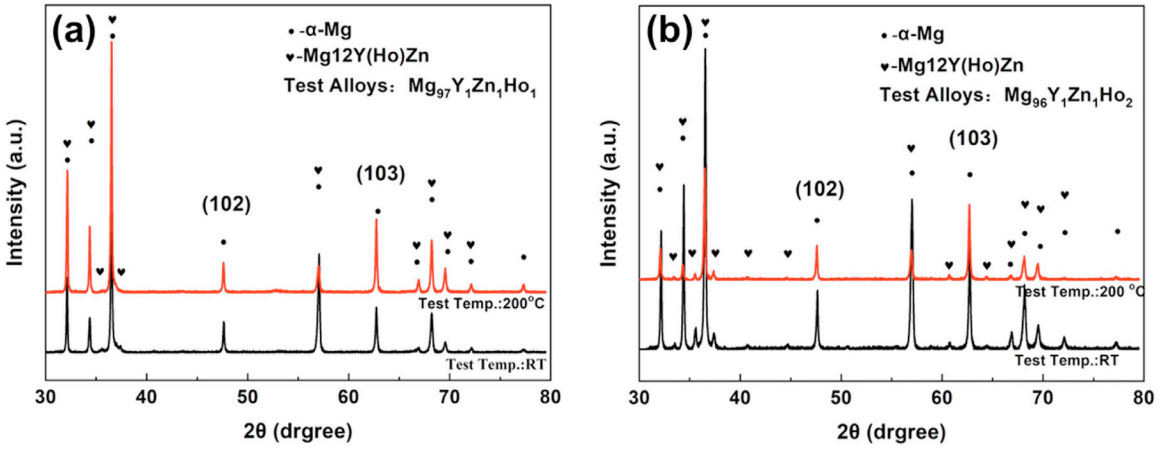

Fig. 9. XRD patterns of the 8%-strained Mg-Y-Zn-Ho alloys.

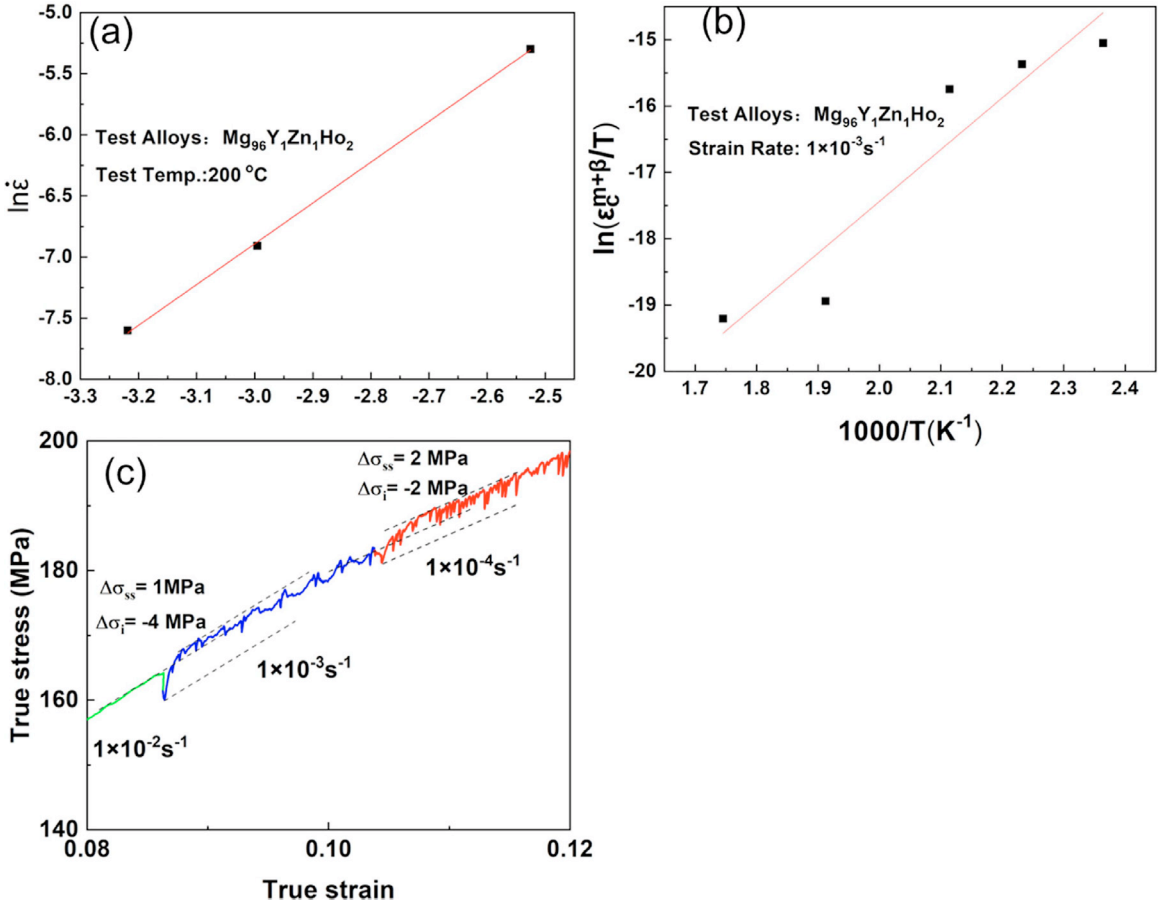

Fig. 10. (a) Variations of critical strains of $Mg_{96}Y_1Zn_1Ho_2$ for the onset of the serrated flow as a function of strain rate, (b) Variations of critical strains of $Mg_{96}Y_1Zn_1Ho_2$ for the onset of the serrated flow as a function of temperature, (c) Results of a representative strain rate jump experiment for $Mg_{96}Y_1Zn_1Ho_2$ alloys.

of the WE54 alloy depends on the migration energy, which is attributed to the diffusivities of Y and Nd in the magnesium matrix. The solubility of Nd in the Mg matrix is low (0.63 at.%), hence its influence on dynamic strain can be neglected. The equation for the diffusion coefficient of Ho and Y in a magnesium matrix calculated via first-principles is as follows [48]:

$$\Phi_{Y\ in\ Mg} = 8.4\ \times 10^{-6} e^{-126987/RT} \tag{4}$$

$$\Phi_{Ho\ in\ Mg} = 1.2\ \times 10^{-6} e^{-119106/RT} \tag{5}$$

where the diffusion coefficients of Y and Ho elements in Mg at 200 °C are 7.56 × 10^{-20} m^2/s and 8.42 × 10^{-20} m^2/s, respectively. Hence, Ho has a higher diffusivity and lower migration energy than Y in the Mg matrix. The high diffusivity and low migration energy of Ho in the Mg matrix contributed to the activation of the DSA effect.

In Fig.1, the tensile curves at different strain rates include regions with and without DSA. The different strain rates result in varying degrees of DSA, so the exponent of the strain rate sensitivity obtained based on Fig. 1 may not be accurate. When the value of ε suddenly decreases, it causes an immediate shift in flow stress, $\Delta\sigma_i$,which is always negative. This shift in the deformation response is indicated by the instantaneous strain rate sensitivity, represented by $m_i = \frac{d\sigma_i}{dln\,\varepsilon}$. However, whether the SRS is negative or positive depends on the steady-state strain rate sensitivity. This involves assessing the variation in the stable flow stress, denoted by $m_s = \frac{d\sigma_{ss}}{dln\,\varepsilon}$, after the strain rate jump [49]. In the DSA regime, when the strain rate jumps from 1 × 10^{-3} s^{-1} to 1 × 10^{-4} s^{-1} under the condition of true strain being 11%, the stress generated ($\Delta\sigma_{SS}$=2 MPa) implies a negative strain rate sensitivity coefficient, as shown in Fig. 10c. This result conforms to the typical DSA effect.

4.2. Dislocation multiplication induced by DSA

For $Mg_{97}Y_1Zn_1Ho_1$ and $Mg_{96}Y_1Zn_1Ho_2$ alloys, the grain size, the volume fraction of the LPSO phase, phase structure is not significantly different, but the content of Ho in the matrix varies enormously, as exhibited in Fig. 6 and Table 1. The tensile curves of the high content of Ho-containing Mg alloys show significant DSA effect during elevated-temperature deformation, while Mg alloys with a low content of Ho just possess weak DSA effect in the late stage of tension, as shown in Fig. 1a. The remarkable DSA effect in the $Mg_{96}Y_1Zn_1Ho_2$ alloy, indicates that the high solid solution of Ho atoms in

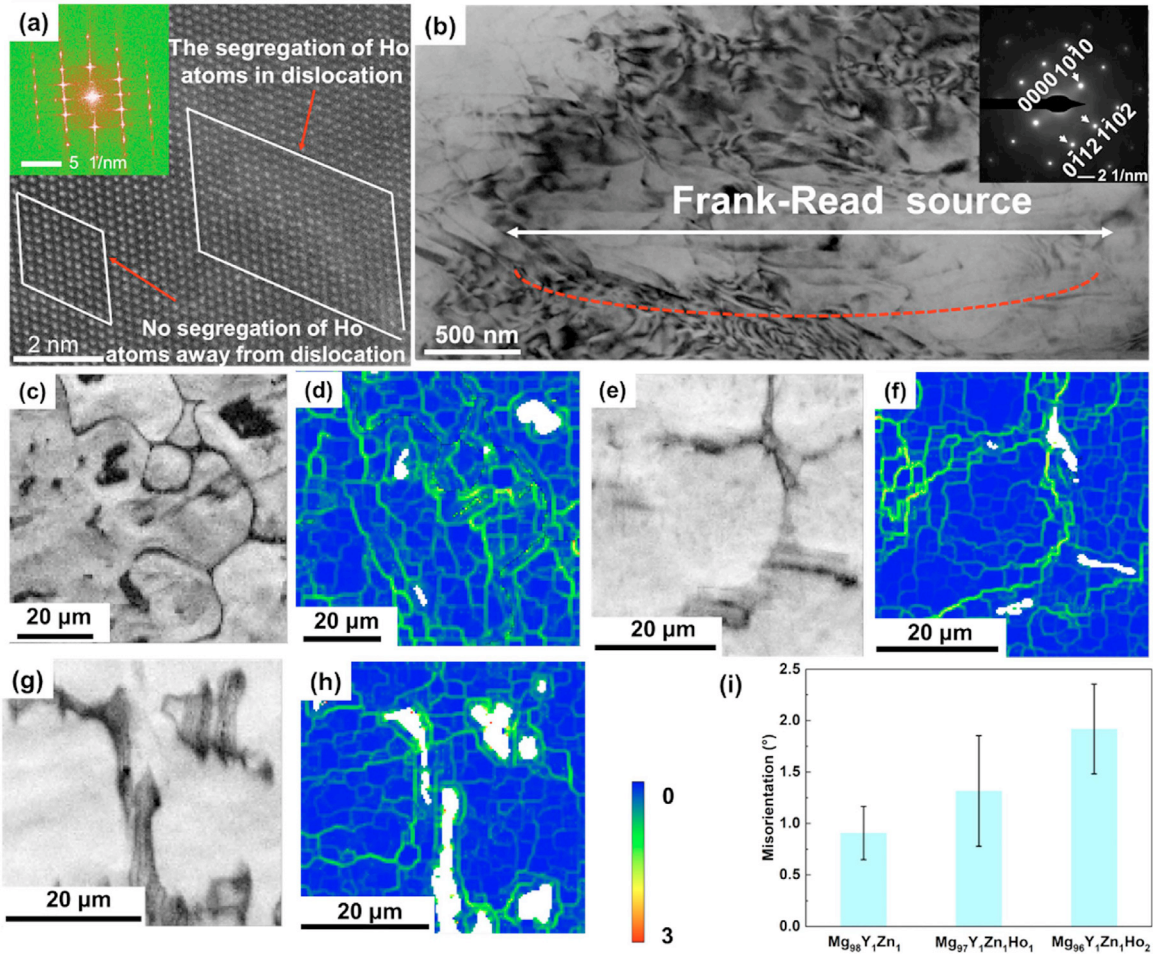

Fig. 11. (a) The atomic-resolution HAADF-STEM images of dislocations in the 8%-strained $Mg_{96}Y_1Zn_1Ho_2$ alloy at 200 °C, imaged under $[2\bar{1}\bar{1}0]$. diffraction conditions. The segregation of Ho atoms at the dislocation core suppresses dislocation motion. (b) The TEM bright-field image of dislocation multiplication through the Frank-Read (FR) source. The Band contrast map and corresponding kernel average misorientation (KAM) map of all alloys deformed by 8% at 200 °C. (c)–(d) $Mg_{98}Y_1Zn_1$, (e)–(f) $Mg_{97}Y_1Zn_1Ho_1$ and (g)-(h) $Mg_{96}Y_1Zn_1Ho_2$ alloy; (i) The statistical misorientation near the LPSO phase indicates that the LPSO phase hinders dislocation movement.

the matrix results in DSA. To examine the interaction between Ho atoms and dislocations, the atomic-scale structure characterization of the 8% pre-tensioned $Mg_{96}Y_1Zn_1Ho_2$ alloy was conducted by the atomic-resolution HAADF-STEM. The contrast of the region containing a pinned dislocation is slightly higher than that of the matrix away from the dislocation, as shown in Fig. 11a, indicating Ho segregation at the dislocation line. Because columnar intensities are proportional to the square of Z (average atomic number) under this imaging mode.

During a dislocation slip, the dislocation segment can be temporarily blocked by obstacles, such as forest dislocations. Before jumping to the next obstacle after overcoming forest dislocations, the blocked dislocation segment may wait for a certain time. During the waiting time, solute atoms tend to diffuse to the core region of the blocked dislocation segment through a short distance [22]. In this experiment, the dislocation morphology is similar to an L or U shape, which matches the shape of a FR source [50], therefore the FR source is activated, as shown in Fig. 11b, the frequent pinning of Ho atoms significantly shortens the length of the statistically average effective FR source. It is reported that the dislocation-generation rate depends on the average effective FR source [51], i.e., $d\rho/d\gamma = 1/bl$, where $d\rho/d\gamma$ is the dislocation-generation rate, l is the average effective FR source. Therefore, the Ho element shortens the average effective FR source through frequent pinning of dislocations, and as a result, promotes the dislocation multiplication.

The traditional DSA effect, caused by atomic pinning and unpinning of dislocations, leads to strain localization, which can reduce the plasticity of the alloy. To uncover new interaction mechanisms between Ho atoms and dislocations to avoid strain localization. Dislocation configurations and dynamic simulations were conducted for analysis. The dislocation configurations under double-beam conditions in the 8%-strained $Mg_{96}Y_1Zn_1Ho_2$ alloy at 200 °C are shown in Fig.12a and b. It is proved that there are $\langle a \rangle$ and $\langle c + a \rangle$ dislocations generated in the $Mg_{96}Y_1Zn_1Ho_2$ alloy during DSA. Based on actual experiment, we simulated the interaction between the Cottrell atmosphere of Ho atoms and dislocations by molec-

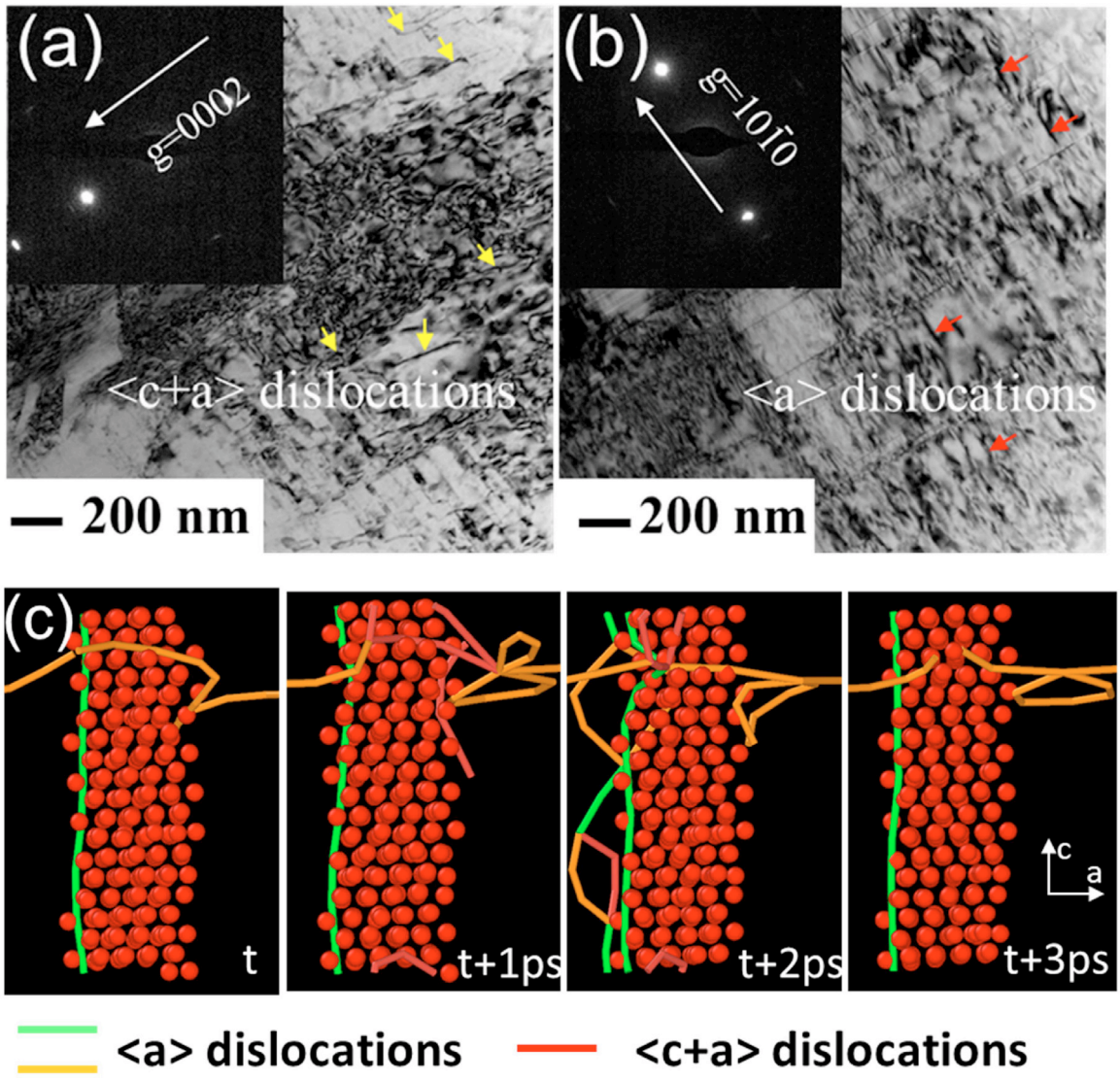

Fig. 12. Dislocation configurations in the 8%-strained $Mg_{96}Y_1Zn_1Ho_2$ alloy at 200 °C. (a) TEM bright-field images viewed with $g = 0002$, (b) TEM bright-field images viewed with $g = 01\bar{1}0$, (a) and (b) are taken from the same region. The zone axis is $[2\bar{1}\bar{1}0]$. (c) The interaction between dislocations and Cottrell atmosphere of Ho atoms during DSA in $Mg_{96}Y_1Zn_1Ho_2$ alloy based on molecular dynamics simulations. The red atoms represent Cottrell atmosphere of Ho atoms.

ular dynamics to further explain the activation mechanism of dislocations, as shown in Fig. 12c. When the movement of $\langle a \rangle$ dislocations is hindered by Cottrell atmosphere, $\langle c + a \rangle$ dislocations are activated, alleviating strain localization, which is consistent with the observations from TEM. Meanwhile, dislocation multiplication phenomenon is also observed. The Cottrell atmosphere of Ho atoms reduce the c/a ratio of the HCP structure, which facilitates the activation of $\langle c + a \rangle$ dislocations [33]. Moreover, the critical shear stress of the slip system decreases with the increase of temperature [52], which is more conducive to activating a greater dislocation density. As a result, the DSA effect in this study mitigates strain localization due to a unique dislocation multiplication mechanism, promoting high strain hardening.

This experiment demonstrates that the activation of $\langle c + a \rangle$ dislocations primarily serve to alleviate the uneven local strains caused by DSA, thereby enhancing significant work hardening capabilities. Numerous studies have shown that Mg-Y-Zn alloy generates $\langle c + a \rangle$ dislocations during elevated-temperature deformation [53]. This is mainly attributed to the Y solute in the matrix promoting the activation of $\langle c + a \rangle$ dislocations. However, in this experiment, the Y content in the matrix is minimal, only 0.2% [45], which is insufficient to activate a significant number of $\langle c + a \rangle$ dislocations. Similar to the results of our team's previous work, only $\langle a \rangle$ dislocations are present [45]. In this experiment, a large amount of Ho elements is solid-soluted in the matrix, forming numerous cottrell atmosphere of Ho atoms that can effectively

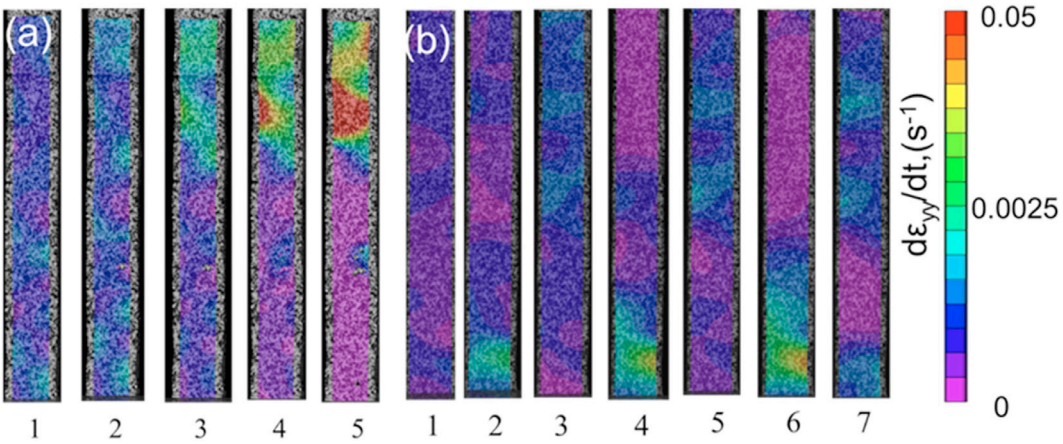

Fig. 13. Series of DIC images of the $Mg_{96}Y_1Zn_1Ho_2$ alloy surface at different temperature. (a) RT and (b) 200 °C.

activate $\langle c + a \rangle$ dislocations and regulate local strains, as shown in Fig. 12. Therefore, based on the current experimental evidence, and the previous work, it is demonstrated that the Cottrell atmosphere of Ho atoms activate $\langle c + a \rangle$ dislocations. Moreover, it is reported that in hexagonal structured alloys, only $\langle a \rangle$ dislocations are activated during DSA, while $\langle c + a \rangle$ dislocations are not activated [54]. In this study, after the addition of Ho element, both $\langle a \rangle$ and $\langle c + a \rangle$ dislocations were observed through TEM and molecular dynamics, as shown in Fig. 8 and Fig. 12. This result also indicates that Ho activates $\langle c + a \rangle$ dislocations.

To further determine the strain uniformity of the DSA effect, DIC analysis was used to in-situ characterize the strain distribution of $Mg_{96}Y_1Zn_1Ho_2$ alloy samples at room temperature and 200 °C, as shown in Fig. 13. The results revealed that at room temperature, stress concentration formed and led directly to fracture (Fig. 13a). However, at 200 °C during deformation, the Ho atoms initially pinned dislocations, forming deformation bands. As the process progressed, the unpinning of Ho atoms and the activation of $\langle c + a \rangle$ dislocations together alleviated strain concentration, promoting the disappearance of deformation bands (Fig.13b). This cyclic motion pattern resulted in relatively uniform deformation during DSA.

The significantly promoted dislocation density of $Mg_{96}Y_1Zn_1Ho_2$ at 200 °C compared with that at RT (Fig. 7d) evidenced that the activation of the DSA at elevated temperatures generated high-density mobile dislocations, and Ho content played a key role in increasing the dislocation density in the Mg-Y-Zn-Ho alloys. Moreover, the $(m+\beta)$ mentioned in Eq. (1) is proportional to the vacancy concentration and mobile dislocation density. Such value $(m+\beta=3.2)$ for the studied $Mg_{96}Y_1Zn_1Ho_2$ is much higher than that in Mg-10 wt.%Ag (1.4) [55] and WE54 alloys (2.2) [47], indicating that there are a large number of dislocations multiplication through DSA in our experiment.

Luo et al. [56,57] reported that the solutes-dislocation interactions can hinder the cross slip of dislocations, resulting in a lower rate of recovery and therefore, a higher rate of dislocation accumulation. In the present work, the dislocation multiplication is enhanced by shortening the average effective FR source, a lower rate of dynamic recovery results from the Ho atoms-dislocation interaction, and the promotion of $\langle c + a \rangle$ dislocation nucleation. As a consequence, high-density dislocations are achieved.

4.3. Deformation mechanisms at elevated temperatures

On the basis of the microstructural analysis, the activation of the DSA and the resultant high-density dislocations are the main mechanism of the strength and ductility increment in Mg-Y-Zn-Ho alloys at elevated temperatures. It is known that LPSO can enhance the tensile strength by hindering the dislocation movement. Meanwhile, the LPSO demonstrated excellent thermal stability even at 500 °C. Therefore, the tensile strength in LPSO-containing Mg alloys can be greatly enhanced at elevated temperatures [58–60]. In current work, the high-density dislocations accumulation and their interactions with the 18R LPSO phase contributed to the enhanced strength. As shown in Fig. 11c-i, with the increase of Ho content, the statistical misorientation near the LPSO phase and interior grains gradually increases, indicating that the Ho promotes the dislocation multiplication and accumulation through DSA and solute-pinning effects during elevated-temperature deformation. It is also found that there are $\langle a \rangle$ and $\langle c + a \rangle$ dislocations generated in the $Mg_{96}Y_1Zn_1Ho_2$ alloy during DSA (Fig. 12), which further enhanced dislocation multiplication. A large number of mobile dislocations motion mainly realizes the high-density dislocation multiplication and accommodates the plastic deformation.

The Kocks-Mecking (KM) model has been widely applied to explain the tensile work hardening characteristics of alloys [61–63]. In this model, the increase in strength due to deformation is determined by the balance between the accumulation and annihilation (rearrangement) of dislocations, which are assumed to combine in an additive manner. The rate of strain hardening can be calculated as:

$$\theta = \theta_0 - K(\sigma - \sigma_y) \tag{6}$$

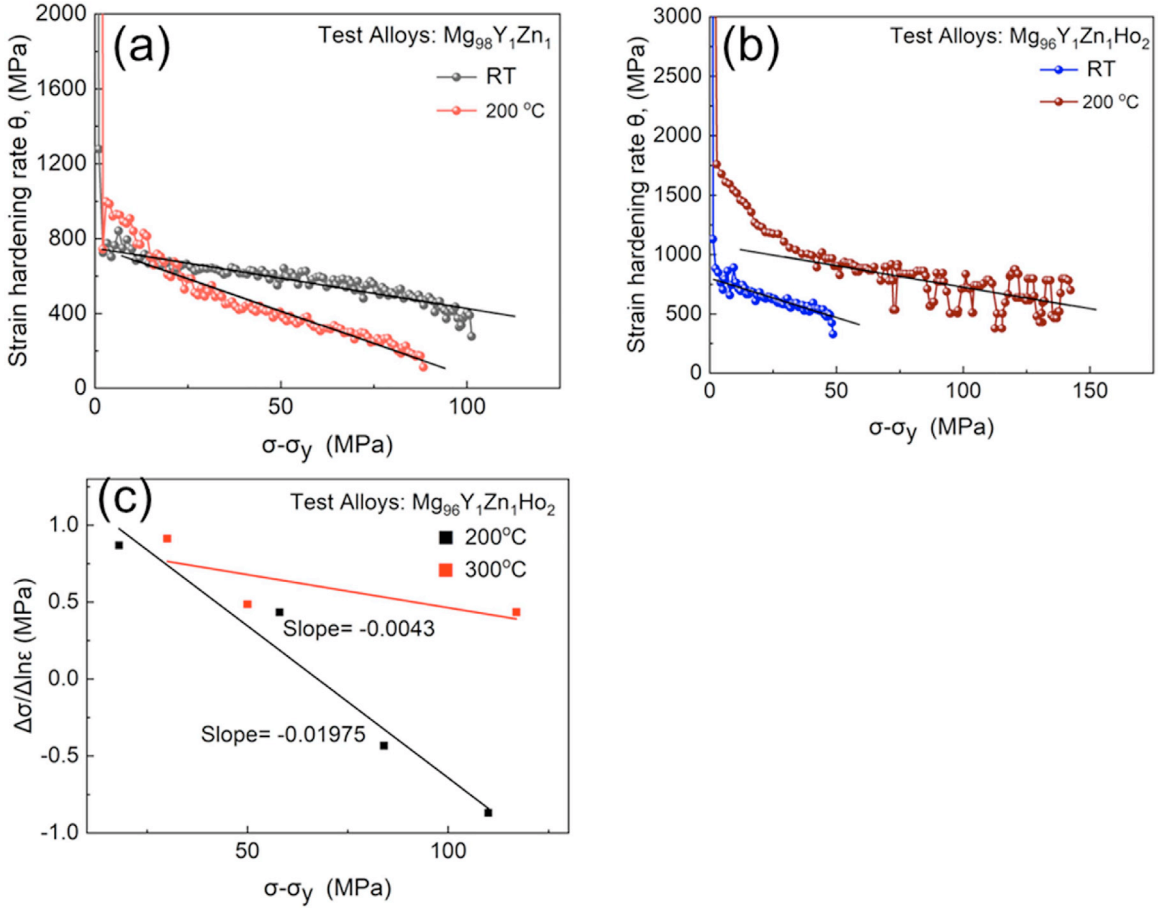

Fig. 14. The strain hardening rate (θ)- effective stress (σ-σ_y) curves for the (a) $Mg_{98}Y_1Zn_1$ alloy, (b) $Mg_{96}Y_1Zn_1Ho_2$ alloy, (c) Haasen plots of the $Mg_{96}Y_1Zn_1Ho_2$ alloy alloys derived from the strain rate change tests at 200 and 300 °C .

Table 2
The intercept and slope of the KM model. The intercept represents dislocation accumulation, and the slope represents dislocation recovery rate.

Alloys		θ_0 (MPa)	K
$Mg_{98}Y_1Zn_1$	RT	750	−3.22
	200 °C	761	−6.95
$Mg_{96}Y_1Zn_1Ho_2$	RT	802	−6.67
	200 °C	1089	−3.63

where θ_0 represents the initial rate of strain hardening, which indicates the rate at which dislocations are stored, while K represents the rate of dynamic recovery. The values of θ_0 and K are shown in Table 2 extracted from Fig. 14a and b. It is found that the strain hardening of $Mg_{98}Y_1Zn_1$ alloy at room temperature exceeds that at 200 °C, while for $Mg_{96}Y_1Zn_1Ho_2$ alloy, the room temperature strain hardening is lower than that at 200 °C. According to the changes in intercept and slope of the KM type plot, it was found that the alloy deformed at 200 °C has high intercept and low slope, which suggests that Mg alloy has high dislocation accumulation and low dislocation recovery rate during dynamic strain, resulting in enhanced strain hardening rate.

Furthermore, to investigate the thermal activation behavior of elevated-temperature deformation, Fig. 14c applies the Haasen plots to describe dislocation strengthening. It is found that the alloys deformed at 200 and 300 °C both exhibit linear behavior, suggesting standard dislocation strengthening under both conditions. The slope of both deformation conditions is negative, which is related to the sensitivity coefficient of negative strain rate [63]. However, it is also observed that during deformation at 300 °C, the slope gradually increases. This is because with the increase in deformation temperature, the activation of dislocations due to DSA becomes easier, further proved the critical effect of DSA on dislocation activity.

The traditional DSA effect can lead to localized softening of the material, causing instability during deformation and ultimately resulting in a decrease in ductility. However, in this work, the Mg-Y-Zn-Ho alloys generating DSA exhibits high ductility. The high-density dislocations induced by DSA effect result in the high strain hardening, which delay necking and improves elongation. In addition, the reduction of stacking fault energy by Ho has been widely reported through simulation calculations and experimental tests [33,62]. The presence of a large amount of Ho elements in the matrix reduces the activation energy of the magnesium alloy. S.

Sandlobes et al. [33] found that the reduction in activation energy is beneficial for the activation of $\langle c + a \rangle$ dislocations. Therefore, the activation of $\langle c + a \rangle$ dislocations also help in alleviating local strains and improve strain hardening. Therefore, both $Mg_{97}Y_1Zn_1Ho_1$ and $Mg_{96}Y_1Zn_1Ho_2$ alloys, the elevated-temperature strength and ductility increase simultaneously compared with their counterparts at RT.

5. Conclusions

In summary, we develop an Mg alloy with excellent elevated-temperature properties by promoting the DSA effects through RE Ho alloying. (1) The influence of Ho on the structures of the Mg alloy and the activation of DSA effects and (2) the effects of the DSA on the enhancement of the elevated-temperature strength and ductility were investigated systematically. The main findings were found, as described below:

(1) A new strategy to break the consensus that dislocation hardening is not suitable for elevated-temperature materials is achieved by DSA effect at elevated-temperature. The addition of Ho promotes the DSA effects during elevated-temperature deformation since Ho is apt to diffuse towards dislocations and pinning their movements. The DSA effects effectively promote the dislocation multiplication, providing a large number of mobile dislocations and suppression of dislocation annihilation. As a result, an excellent combination of strength and ductility is obtained in Mg alloys.
(2) The high tensile strength (230 MPa) and elongation (21%) in the as-cast Mg-Y-Zn-Ho alloys undergoing DSA are obtained at 200 °C. The strengths and ductility of the alloys at elevated temperatures were much higher than that at RT (179 MPa and 9%, respectively), confirming the DSA strengthening strategy is suitable for improvement of elevated-temperature strength and ductility.
(3) The addition of Ho did not affect the structures and properties of the LPSO phase but increased the volume fraction of the LPSO phase and the hardness of the alloy matrix, contributing to the enhancement of the strength through LPSO-second-phase strengthening and solid-solution strengthening.
(4) The high-density dislocations accumulation and their interactions with the 18R LPSO phase contributed to the enhanced strength. The high-density dislocations result in high strain hardening, which delay necking and improves elongation.

Declaration of competing interest

The authors declare that they have no known competing financial interests or personal relationships that could have appeared to influence the work reported in this paper.

Qian Li is an editorial board member/editor-in-chief for Journal of Magnesium and Alloys and was not involved in the editorial review or the decision to publish this article. All authors declare that there are no competing interests.

CRediT authorship contribution statement

Mingyu Fan: Formal analysis, Data curation, Writing – original draft. **Ye Cui:** Formal analysis, Writing – review & editing. **Xin Zhou:** Formal analysis, Data curation. **Junming Chen:** Conceptualization, Formal analysis. **Yang Zhang:** Formal analysis, Data curation. **Lixin Sun:** Formal analysis, Data curation. **Jamieson Brechtl:** Formal analysis, Data curation. **Daqing Fang:** Formal analysis. **Qian Li:** Formal analysis, Data curation. **Qingqing Ding:** Formal analysis, Data curation. **Hongbin Bei:** Formal analysis. **Peter K. Liaw:** Formal analysis, Data curation. **Yanzhuo Xue:** Formal analysis, Writing – review & editing. **Xun-Li Wang:** Formal analysis, Supervision, Funding acquisition. **Yang Lu:** Formal analysis, Writing – review & editing. **Zhongwu Zhang:** Conceptualization, Formal analysis, Supervision, Funding acquisition, Writing – review & editing.

Acknowledgments

The present work was supported by the National Key Research and Development Project (2023YFA1609100), the NSFC Funding (U2141207, 52171111, 52001083) and Natural Science Foundation of Heilongjiang (YQ2023E026), China Postdoctoral Science foundation (2024M754149), Postdoctoral Fellowship Program of CPSF (GZC20242192). YL thanks Hong Kong RGC general research fund (#11200623) and HKU Seed Fund for Collaborative Research (#2207101618). PKL thanks the support from the National Science Foundation (DMR-1611180 and 1809640) with the program directors, Drs. J. Madison, J. Yang, G. Shiflet and D. Farkas. XLW acknowledges the support by Croucher Senior Research Fellowship and CityU Project (Project No. 9229019), Shenzhen Science and Technology Program (Project No. JCYJ20220818101203007).

References

[1] D.F. Shi, C.M. Cepeda-Jiménez, M.T Pérez-Prado, J. Magnes. Alloys 10 (1) (2022) 224–238.
[2] B.B. He, B. Hu, H.W. Yen, G.J. Cheng, Z.K. Wang, H.W. Luo, M.X. Huang, Science 357 (2017) 1029.
[3] S.R. Agnew, A. Singh, C.A. Calhoun, R.P. Mulay, J.J. Bhattacharyya, H. Somekawa, T. Mukai, B. Clausen, P.D. Wu, Int. J. Plast. 100 (2018) 34–51.
[4] J. Han, J. Sun, Y. Song, B. Xu, Z. Yang, S. Xu, Y. Han, G. Wu, J. Zhao, J. Magnes. Alloys 11 (7) (2023) 2392–2403.
[5] Y.Z. Zhang, J. Xie, J. Zhang, X.-S. Yang, R. Wu, J. Magnes. Alloys 12 (5) (2024) 1774–1791.
[6] W. Fu, Y. Huang, J. Sun, A.H.W. Ngan, Int. J. Plast. 154 (2022) 103296.
[7] C. Yan, Y. Xin, X.B. Chen, D. Xu, P.K. Chu, C. Liu, B. Guan, X. Huang, Q. Liu, Nat Commun 12 (2021) 4616.
[8] S. Jiang, H. Wang, Y. Wu, X. Liu, H. Chen, M. Yao, B. Gault, D. Ponge, D. Raabe, A. Hirata, M. Chen, Y. Wang, Z. Lu, Nature 544 (2017) 460–464.
[9] S.S. Xu, J.P. Li, Y. Cui, Y. Zhang, L.X. Sun, J. Li, J.H. Luan, Z.B. Jiao, X.L. Wang, C.T. Liu, Z.W. Zhang, Int. J. Plast. 128 (2020) 102677.

[10] G.I. Taylor, Proc. R. Soc. Lond. 145 (1934) 362–387.
[11] J. Kan, Z. Ding, X. Chen, H. Hou, Y. Zhao, W. Liu, J. Magnes. Alloys (2024) (In press), doi:10.1016/j.jma.2024.11.009.
[12] H.T. Jeong, W.J. Kim, J. Magnes. Alloys 10 (10) (2022) 2901–2917.
[13] Q. Pan, L. Zhang, R. Feng, Q. Lu, K. An, A.C. Chuang, J.D. Poplawsky, P.K. Liaw, L. Lu, Science 374 (2021) 984–989.
[14] Z. Li, Y. Cui, W. Yan, D. Zhang, Y. Fang, Y. Chen, Q. Yu, G. Wang, H. Ouyang, C. Fan, Q. Guo, D.-B. Xiong, S. Jin, G. Sha, N. Ghoniem, Z. Zhang, Y.M. Wang, Mater. Today 50 (2021) 79–88.
[15] X. Zhang, A. Godfrey, X. Huang, N. Hansen, Q. Liu, Acta Mater 59 (2011) 3422–3430.
[16] B. Babu, L.-E. Lindgren, Int. J. Plast. 50 (2013) 94–108.
[17] W. Huo, F. Fang, H. Zhou, Z. Xie, J. Shang, J. Jiang, Scr. Mater. 141 (2017) 125–128.
[18] A.A. Abildina, A.P. Kurbatov, Y.G. Bakhytzhan, R.Z. Jumanova, A.M. Argimbayeva, K. Avchukir, G.S. Rakhymbay, J. Magnes. Alloys 11 (6) (2023) 2125–2141.
[19] C. Ye, S. Suslov, B.J. Kim, E.A. Stach, G.J. Cheng, Acta Mater 59 (2011) 1014–1025.
[20] S.K. Woo, R. Pei, T. Al-Samman, D. Letzig, S. Yi, J. Magnes. Alloys 10 (1) (2022) 146–159.
[21] K. Peng, W. Chen, K. Qian, Mater. Sci. Eng. A 415 (2006) 53–58.
[22] W.A. Curtin, D.L. Olmsted, L.G. Hector, Nat. Mater. 5 (2006) 875–880.
[23] M.A. Soare, W.A. Curtin, Acta Mater 56 (2008) 4046–4061.
[24] H. Ovri, J. Magnes. Alloys 11 (5) (2023) 1643–1655.
[25] A.M. Beese, Z. Wang, A.D. Stoica, D. Ma, Nat Commun 9 (2018) 2083.
[26] M.H. Lee, J.H. Kim, B.K. Choi, Y.H. Jeong, J. Alloys Compd. 428 (2007) 99–105.
[27] H. Aboulfadl, J. Deges, P. Choi, D. Raabe, Acta Mater 86 (2015) 34–42.
[28] J. Brechtl, S.Y. Chen, X. Xie, Y. Ren, J.W. Qiao, P.K. Liaw, S.J. Zinkle, Int. J. Plast. 115 (2019) 71–92.
[29] Y. Zhang, J.P. Liu, S.Y. Chen, X. Xie, P.K. Liaw, K.A. Dahmen, J.W. Qiao, Y.L. Wang, Prog. Mater. Sci. 90 (2017) 358–460.
[30] L. Gao, R.S. Chen, E.H. Han, J. Alloys Compd. 472 (2009) 234–240.
[31] X.Y. Fang, D.Q. Yi, J.F. Nie, Metall. Mater. Trans. A 40 (2009) 2761.
[32] W.H. Wang, D. Wu, R.S. Chen, X.N. Zhang, J. Mate. Sci. Technol. 34 (2018) 1236–1242.
[33] S. Sandlöbes, Z. Pei, M. Friák, L.F. Zhu, F. Wang, S. Zaefferer, D. Raabe, J. Neugebauer, Acta Mater 70 (2014) 92–104.
[34] T. Kusama, T. Omori, T. Saito, S. Kise, T. Tanaka, Y. Araki, R. Kainuma, Nat Commun 8 (2017) 354.
[35] G. Farkas, I. Groma, J. Vesely, K. Mathis, J. Appl. Crystallogr. 53 (2) (2020) 360–368.
[36] I. Groma, Phy. Rev. B 57 (13) (1998) 7535–7542.
[37] J. Gubicza, K. Máthis, P. Nagy, P. Jenei, Z. Hegedűs, A. Farkas, J. Veselý, S.-i. Inoue, D. Drozdenko, Y. Kawamura, J. Magnes. Alloys 12 (5) (2024) 2024–2040.
[38] M. Fan, Y. Cui, Y. Zhang, X. Wei, X. Cao, P.K. Liaw, Y. Yang, Z. Zhang, J. Magnes. Alloys 11 (4) (2023) 1321–1331.
[39] G. Xie, F. Wang, X. Lai, Z. Xu, X. Zeng, Int. J. Mech. Sci. 250 (2023) 108320.
[40] A. Stukowski, Modell. Simulat. Mat. Sci. Engineer. 18 (2010) 015012.
[41] R. Ahmad, Z. Wu, S. Groh, W.A. Curtin, Scr. Mater. 155 (2018) 114–118.
[42] S. Zhu, M.A. Easton, T.B. Abbott, J.-F. Nie, M.S. Dargusch, N. Hort, M.A. Gibson, Metall. Mater. Trans. A 46 (2015) 3543–3554.
[43] C. Zheng, S. Chen, M. Cheng, S. Zhang, Y. Li, Y. Yang, J. Magnes. Alloys 11 (11) (2023) 4218–4234.
[44] K. Kishida, K. Nagai, A. Matsumoto, A. Yasuhara, H. Inui, Acta Mater 99 (2015) 228–239.
[45] M. Fan, Z. Zhang, Y. Cui, L. Liu, Y. Liu, P.K. Liaw, Int. J. Plast. 163 (2023) 103558.
[46] P.G. McCormigk, Acta Mater 20 (1972) 351–354.
[47] S.M. Zhu, J.F. Nie, Scr. Mater. 50 (2004) 51–55.
[48] W. Zhong, J.-C. Zhao, Acta Mater 201 (2020) 191–208.
[49] S. Zhao, C. Meng, F. Mao, W. Hu, G. Gottstein, Acta Mater 76 (2014) 54–67.
[50] Pergamon, Dislocation Multiplication, Exhaustion and Work-hardening, in: D. Caillard, J.L. Martin (Eds.), Pergamon materials series, 8, Pergamon, 2003, pp. 323–360, doi:10.1016/S1470-1804(03)80039-1.
[51] Y.N. Cui, P. Lin, Z.L. Liu, Z. Zhuang, Int. J. Plast. 55 (2014) 279–292.
[52] M.R. Barnett, Metall. Mater. Trans. A 34 (2003) 1799–1806.
[53] K. Fekete, G. Farkas, D. Drozdenko, D. Tolnai, A. Stark, P. Dobroň, G. Garcés, K. Máthis, Intermetallics 138 (2021) 107321.
[54] P. Agrawal, S. Karthikeyan, S.K. Makineni, B. Gault, D. Banerjee, Acta Mater 222 (2022) 117436.
[55] M.C. Chaturvedi, D.J. Lloyd, Philo. Mag. 30 (1974) 1199–1207.
[56] Z.C. Luo, M.X. Huang, Scr. Mater. 178 (2020) 264–268.
[57] Z.C. Luo, M.X. Huang, Scr. Mater. 142 (2018) 28–31.
[58] K. Hagihara, Z. Li, M. Yamasaki, Y. Kawamura, T. Nakano, Acta Mater 163 (2019) 226–239.
[59] K. Hagihara, T. Mayama, M. Yamasaki, S. Harjo, T. Tokunaga, K. Yamamoto, M. Sugita, K. Aoyama, W. Gong, S. Nishimoto, Int. J. Plast. 173 (2024) 103865.
[60] T. Mayama, S.R. Agnew, K. Hagihara, K. Kamura, K. Shiraishi, M. Yamasaki, Y. Kawamura, Int. J. Plast. 154 (2022) 103294.
[61] H.T. Jeong, W.J. Kim, Mater. Sci. Eng. A 794 (2020) 139862.
[62] Z. Pei, D. Ma, M. Friák, B. Svendsen, D. Raabe, Phys. Rev. B 92 (2015).
[63] D. Zhou, X. Zhang, H. Wang, Y. Li, B. Sun, D. Zhang, Int. J. Plast. 157 (2022) 103405.